J. Fluid Mech. (2014), *vol.* 752, *pp.* 410–438. © Cambridge University Press 2014
doi:10.1017/jfm.2014.341

Ejecta evolution during cone impact

J. O. Marston[1,†] and S. T. Thoroddsen[1,2]

[1]Division of Physical Sciences and Engineering, King Abdullah University of Science and Technology, Thuwal 23955-6900, Saudi Arabia

[2]Clean Combustion Research Center, King Abdullah University of Science and Technology, Thuwal 23955-6900, Saudi Arabia

(Received 6 March 2014; revised 4 June 2014; accepted 11 June 2014)

We present findings from an experimental investigation into the impact of solid cone-shaped bodies onto liquid pools. Using a variety of cone angles and liquid physical properties, we show that the ejecta formed during the impact exhibits self-similarity for all impact speeds for very low surface tension liquids, whilst for high-surface tension liquids similarity is only achieved at high impact speeds. We find that the ejecta tip can detach from the cone and that this phenomenon can be attributed to the air entrainment phenomenon. We analyse of a range of cone angles, including some ogive cones, and impact speeds in terms of the spatiotemporal evolution of the ejecta tip. Using superhydrophobic cones, we also examine the entry of cones which entrain an air layer.

Key words: contact lines, interfacial flows (free surface), jets

1. Introduction

The idealised impact of a cone-shaped solid body onto water is a fascinating example of a fluid flow problem with no external length scale. It is also a practically relevant geometry for studying the origins of the splash induced during ship-slamming (Faltinsen 1990), where a key consideration is the hydrodynamic load acting on the wetted portion of the ship, which arises from the liquid sheet (ejecta) attached to the hull. Furthermore, there has been a long-standing interest in the kinematics of thin ejecta sheets in a variety of impact configurations, namely sphere impacts onto water (Thoroddsen *et al.* 2004; Duez *et al.* 2007), sphere impact into granular beds (Marston, Li & Thoroddsen 2012*a*; Marston, Vakarelski & Thoroddsen 2012*b*), liquid drop impacts onto pools (Thoroddsen 2002; Josserand & Zaleski 2003; Thoroddsen *et al.* 2011; Zhang *et al.* 2011; Thoraval *et al.* 2012), thin films (Weiss & Yarin 1999) and solid surfaces (Yarin & Weiss 1995; Sikalo *et al.* 2002; Xu, Zhang & Nagel 2005), jets striking flat plates (e.g. Clanet & Villermaux 2002). Thus, we seek to complement these studies with information of the ejecta sheet in an experiment without an external length scale. It is also intended that observations from this experimental study can help guide some new theoretical developments of cone impact.

---

† Present address: Department of Chemical Engineering, Texas Tech University, Lubbock, TX 79409-3121, USA. Email address for correspondence: jeremy.marston@kaust.edu.sa

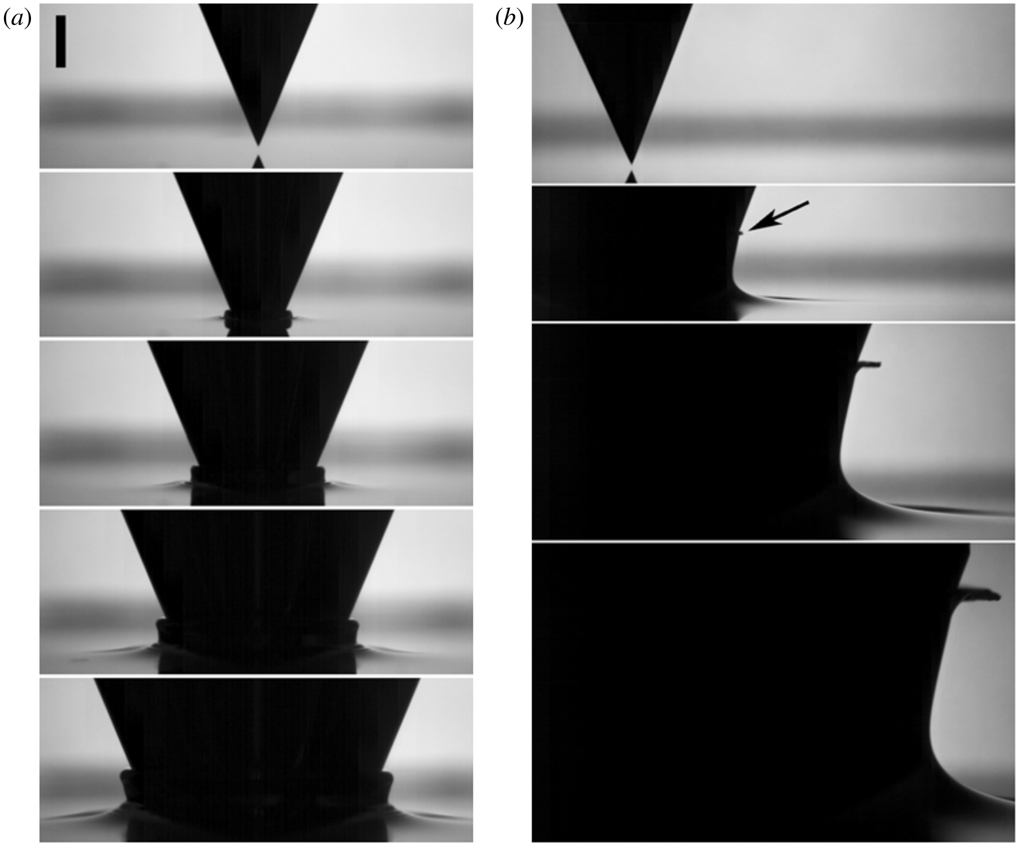

FIGURE 1. Image sequences from a high-speed video of a 45° cone impacting vertically onto quiescent surfaces of water (*a*) with speed of 1.36 m s^{-1} and PP1 (*b*) with speed of 4.24 m s^{-1}, showing the qualitative difference in ejecta shapes. The time between images is 4.2 ms (*a*) and 3.6 ms (*b*). The reference scale bar is 5 mm. See also online supplementary movies 1 and 2.

In the absence of gravity, viscosity and surface tension, the geometrically self-similar shape of a cone makes it likely that the flow also becomes self-similar. Therefore, for the real experimental situation where these three forces are not negligible, an obvious question arises: what governs the initial motion of the ejecta along the cone and to what extent is it self-similar? Two experimental examples of the same cone impacting onto water and perfluorohexane (PP1) are shown in figure 1 (see also online supplementary movies 1 and 2 available at http://dx.doi.org/10.1017/jfm.2014.341). The two impact velocities show different ejecta shapes and are therefore not universal. Herein we seek to characterise the underlying mechanisms at play in this phenomenon.

Specific to cone impact events, previous experimental and theoretical studies in this area have mainly focused on the two-dimensional entry problem using wedges, rather than the three-dimensional case of a cone. Specific studies pertaining to self-similarity include those of Mackie (1969), who used the similarity variables $x/(Vt)$ and $y/(Vt)$ to present a closed-form solution of the free-surface elevation in his analysis of two-dimensional wedge impact, where V is the impact velocity and t the time from first contact. Hughes (1972) investigated the entry of a 90° wedge into water. His experiments supported his arguments that the influence of gravity should be relatively small and that the fluid motion should exhibit self-similarity during high-speed entry. Furthermore, Greenhow (1987) argued that high-speed entries are expected to be self-similar since, locally, the fluid acceleration will be much greater than gravity. In particular, gravity is negligible if $t \leqslant V/(2g)$. Recently, Moore *et al.* (2012, 2013) have extended the classical theory of Wagner to examine three-dimensional oblique impacts for small deadrise angles to calculate the pressure field and behaviour of the 'splash sheet'. For further reviews of the theoretical treatment of this problem, we refer the reader to the papers of Greenhow (1987), Korobkin & Pukhnachov (1988), Howison, Ockendon & Wilson (1991), Scolan & Korobkin (2001), Moore *et al.* (2012) and Iafrati & Korobkin (2004), whilst we restrict our attention hereafter to the experimental studies.

One of the earliest studies of true cone impacts is by Baldwin (1971), who performed experiments for a range of cone angles and impact speeds, however, the emphasis is placed on deriving impact forces (through an embedded accelerometer) and drag coefficients. Lewis *et al.* (2010) performed an experimental investigation of a 25° wedge impact using synchronised acquisition of video, pressure and acceleration measurements in order to assess the pressure distribution along the wedge surface along with the jet evolution. We note, however, that the temporal and spatial resolution of their set-up was insufficient to capture the very early motion of the ejecta, which is essential to provide useful quantitative information for testing numerical and theoretical studies of this process.

Oblique impacts of wedges with calm water surfaces were also studied by Judge, Troesch & Perlin (2004) and Semenov & Yoon (2009), both concerned with the fluid detachment from the trailing edge of the wedge. Their experiments, however, also lacked the necessary spatial and temporal resolution to look at the finer details of the early ejecta motions.

El Malki Alaoui *et al.* (2012) used cones in an experimental study of water entry, however, the main focus of their experiment was the derivation of slamming coefficients. Prior to that, De Backer *et al.* (2009) used high-speed video to study the impact of both hemispheres and cones onto water, where they observed that the jet flow, initially attached to the surface, detached relatively quickly from the hemisphere. In contrast, the jet remained attached to the cones, whereupon a wetting factor was deduced and compared to Wagner's theory for two-dimensional jet flow, with a typical deviation of approximately 20 %.

The overall aim of this study is to provide extensive quantitative measurements of the early ejecta evolution during the impact of cones onto quiescent liquid surfaces using high-speed videography. By using a range of cone angles and liquid properties, and a set-up which produces a constant speed during the impact, we can also fully test the conditions under which self-similar motions arise.

2. Experimental set-up and protocol

2.1. *Cones, liquids and surface treatment*

The experimental set-up is shown schematically in figure 2. We use a piston operated by compressed air at pressures up to eight bar to drive the motion of the cone. The piston is mounted vertically on an optical rail which also allows us to vary the initial height of the piston above the free surface of the liquid. The cone thus impacts vertically with speed $V_c \leqslant 5$ m s^{-1}. The use of a piston ensures that the speed of

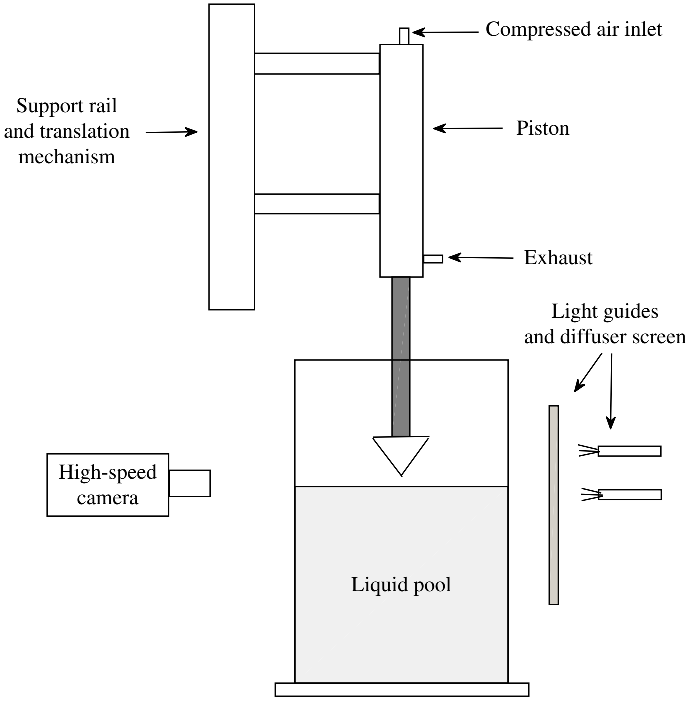

FIGURE 2. Schematic of the experimental set-up used.

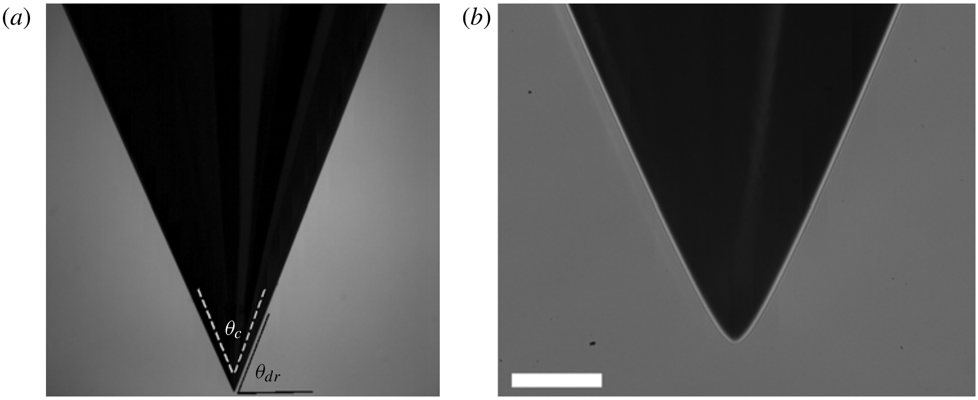

FIGURE 3. (*a*) Image of the cone showing the cone angle, θ_c, and the deadrise angle, θ_{dr}. (*b*) Image of the cone tip at 10× optical magnification for cone angle of 45°. The scale bar is 200 µm.

the cone during penetration through the free surface is constant. The cone itself is securely attached directly to the piston shaft.

The cone angle, θ_c, is defined as the full opening angle of the cone and the angle of the cone surface from the undisturbed free surface is the deadrise angle, $\theta_{dr} = \pi/2 - \theta_c/2$. These are defined graphically in figure 3(*a*), while figure 3(*b*) shows an image of the cone tip at 10× optical magnification for $\theta_c = 45°$. The cones were custom-made

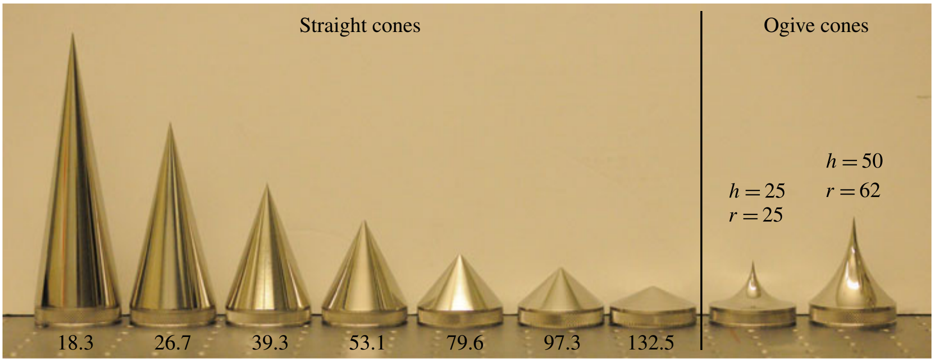

FIGURE 4. Photograph of all of the cones used in this study, including seven straight cones and two curved cones. The cone angle for the straight cone is given below each cone, whilst for the curved cones, the height and radius of curvature are given.

Fluid (—)	Viscosity μ (mPa s)	Density ρ (kg m^{-3})	Surface tension σ (mN m^{-1})	Air entrainment speed V_{ae} (m s^{-1})
Pure water	0.96	996	72	14.5
50 % glycerol	8.1	1146	68	2.81
75 % glycerol	52	1208	66.4	0.67
16 % ethanol	2.2	966	48.1	5.75
50 % ethanol	2.9	854	30.2	3.21
PP1	1.1	1710	11.9	2.99

TABLE 1. Physical properties of the fluids used in the experiments. The stated glycerol and ethanol concentrations are volume fractions in water. The values of V_{ae} are calculated using (3.1).

(TSE Troller AG, Switzerland) from stainless steel and precision ground to a mirror-like finish with average surface roughness $R_a < 1$ µm, determined by atomic force microscopy. In addition to the 45° cone, a range of cone angles were tested for the straight-edge cones with $\theta_c = 18.3$, 26.7, 39.3, 53.1, 79.6, 97.3 and 132.5, as well as two ogive conical shapes, resembling trumpets, with heights from base-to-tip of 25 and 50 mm and radii of curvature $r = 25$ and 62 mm. High-magnification images of the tips of these two cones indicates that the tip has a flat part approximately 400 µm wide with an extrapolated tip angle of approximately 16°. All cones have a base diameter of 50 mm. A photograph of the full set of cones tested is shown in figure 4.

The liquids used in this study, listed in table 1, were chosen to yield a range of physical properties. Water/glycerin mixtures were used to vary the viscosity, whereas water/ethanol mixtures were used to change the surface tension. Very low surface tension was achieved using PP1 (C_6F_{14}). All of the experiments were carried out in an air-conditioned laboratory at 21 °C. For impact onto water, we also performed a series of experiments where the cone surface was modified to yield a superhydrophobic surface. The hydrophobising agent used was a commercially available product, Glaco Mirror-coat ‘Zero’ (Soft 99 Co., Japan), which is an alcohol-based suspension of silica nanoparticles. The entire cone was immersed in the agent for several seconds and then removed and allowed to air-dry before testing. This agent is known to yield superhydrophobic surfaces, whereby a water droplet will exhibit an apparent contact angle of more than 160° (Vakarelski *et al.* 2012). When slowly immersed in water, the coated cone entrains a full air layer, commonly referred to as a plastron (Shirtcliffe *et al.* 2006).

2.2. *Image capture and analysis*

The impact events were captured using one of two high-speed video cameras (Photron Fastcam SA-5 or Phantom V1610) operating at frame rates of up to 15 000 f.p.s. We used a back-lighting system employing fibre-optic light guides and a diffuser screen to achieve silhouette imaging. For the Photron system, the camera was triggered manually, whilst for the Phantom system, we used the image-based auto trigger (IBAT) function to trigger the recording. The images captured were of sufficiently high contrast to enable custom-written image analysis routines in Matlab to find the ejecta edge and tip at each frame. As such, we were able to extract the overall shape of the liquid free surface at each frame and both the radial and vertical position of the ejecta tip (i.e. contact line) relative to the impact point of the cone. A limited set of experiments used a prototype of the Shimadzu hypervision camera developed by Etoh *et al.* (2003), at frame rates up to 50 000 f.p.s.

2.3. *Geometrical considerations and parameter space*

In the absence of an external length scale, dimensional analysis leads to just two dimensionless groups, namely the Capillary number and a physical properties number:

$$Ca = \frac{\mu V_c}{\sigma}, \quad N_{pp} = \frac{g\mu^4}{\rho\sigma^3}. \tag{2.1a,b}$$

For the experiments described herein, our parameter ranges were as follows:

$$0.017 \leqslant Ca \leqslant 4.1, \quad 2.64 \times 10^{-11} \leqslant N_{pp} \leqslant 2.03 \times 10^{-4}. \tag{2.2a,b}$$

However, for our experiments, the ejecta typically travels the entire vertical length of the cone (up to 15 cm) in 10–20 ms, depending on the cone angle and speed. Over this short time scale, the typical extent of motion due to gravitational forces, $\frac{1}{2}gt^2 < 2$ mm, is in most cases at least an order of magnitude smaller than the distance travelled by the ejecta tip. In addition, the thickness of the liquid film on the cone rarely exceeds the capillary length, $a = \sqrt{\sigma/(\rho g)}$ and for the video sequences presented herein $t < V_c/(2g)$. Thus, we will neglect gravitational forces in our analysis. Note, however, that for the lowest cone angle with $\theta_c = 18.3°$, a typical time scale for the length of the cone to penetrate fully into the tank is approximately 100 ms, whereby $\frac{1}{2}gt^2 \approx 5$ cm, whilst the length of the cone is 15.7 cm. Therefore, for the lowest cone angle and impact speeds, gravity will become important in the evolution dynamics.

As such, in order to scale our data, we need to define a time-dependent length scale, $L(t)$. One possibility is the geometrical length scale defined in figure 5, which is the radial (horizontal) distance from the axis of symmetry to the intersection of the cone with the undisturbed initial free surface. Simple geometrical arguments dictate that this is given by

$$L_s(t) = tV_c \tan\left(\frac{\theta_c}{2}\right), \quad L_c(t) = r - \sqrt{r^2 - (tV_c)^2}, \tag{2.3a,b}$$

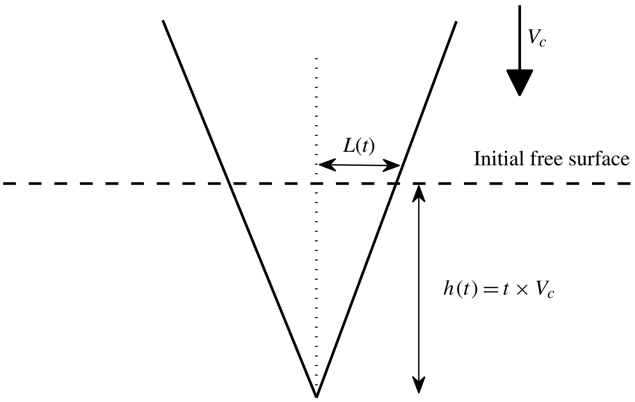

FIGURE 5. Definition of time-dependent length scale, $L(t)$, measured from the axis of symmetry to the intersection of the cone edge with the undisturbed initial free surface.

for straight and curved cones, respectively. If the ejecta sheet were to be dominated purely by viscous effects, the relevant length scale would be $L_\nu=\sqrt{\nu t}$, which may be the case for the highest viscosity solution used herein ($\mu=52$ mPa s), however, for most cases the ejecta thickness $\delta\gg L_\nu$.

We also neglect the possibility of cavitation taking place during the impact, as

$$C_n=\frac{p-p_v}{0.5\rho_l V_c^2}>3, \tag{2.4}$$

even for the highest vapour pressure which occurs for the PP1 liquid.

3. Experimental observations for fixed cone angle $\theta_c=45^\circ$

3.1. *Influence of impact speed*

Figure 6 shows image sequences from impact experiments onto water, at different cone impact speeds of (*a*) $V_c=1.26$ m s^{-1}, (*b*) $V_c=2.16$ m s^{-1}, (*c*) $V_c=3.21$ m s^{-1} and (*d*) $V_c=4.95$ m s^{-1}. Two basic observations can immediately be made. First, the ejecta tip (hereafter also referred to as the contact line, notwithstanding the possibility of an entrained air layer) moved further up the cone with increasing impact speed; this is clear from visual inspection of the last frames in each sequence noting also that the time intervals for each respective sequence decreases, so that the cone has penetrated about the same distance into the pool in each vertical column of the figure. Second, the ejecta is thinner for high impact velocities and the tip is much more pronounced for low-speed impacts. In the final frames in each sequence we estimate the thickness of the tip, normal to the cone surface, to be (*a*) 1800 μm, (*b*) 960 μm, (*c*) 560 μm and (*d*) 360 μm. Based on pixel resolution, the accuracy of these estimates are to within ±80 μm.

3.2. *Influence of surface tension*

For a solid surface (e.g. a tensioned tape) plunging into a liquid pool as in a dip coating operation, many studies have reported correlations for the entrainment threshold velocity above which air will become incorporated into the contact line

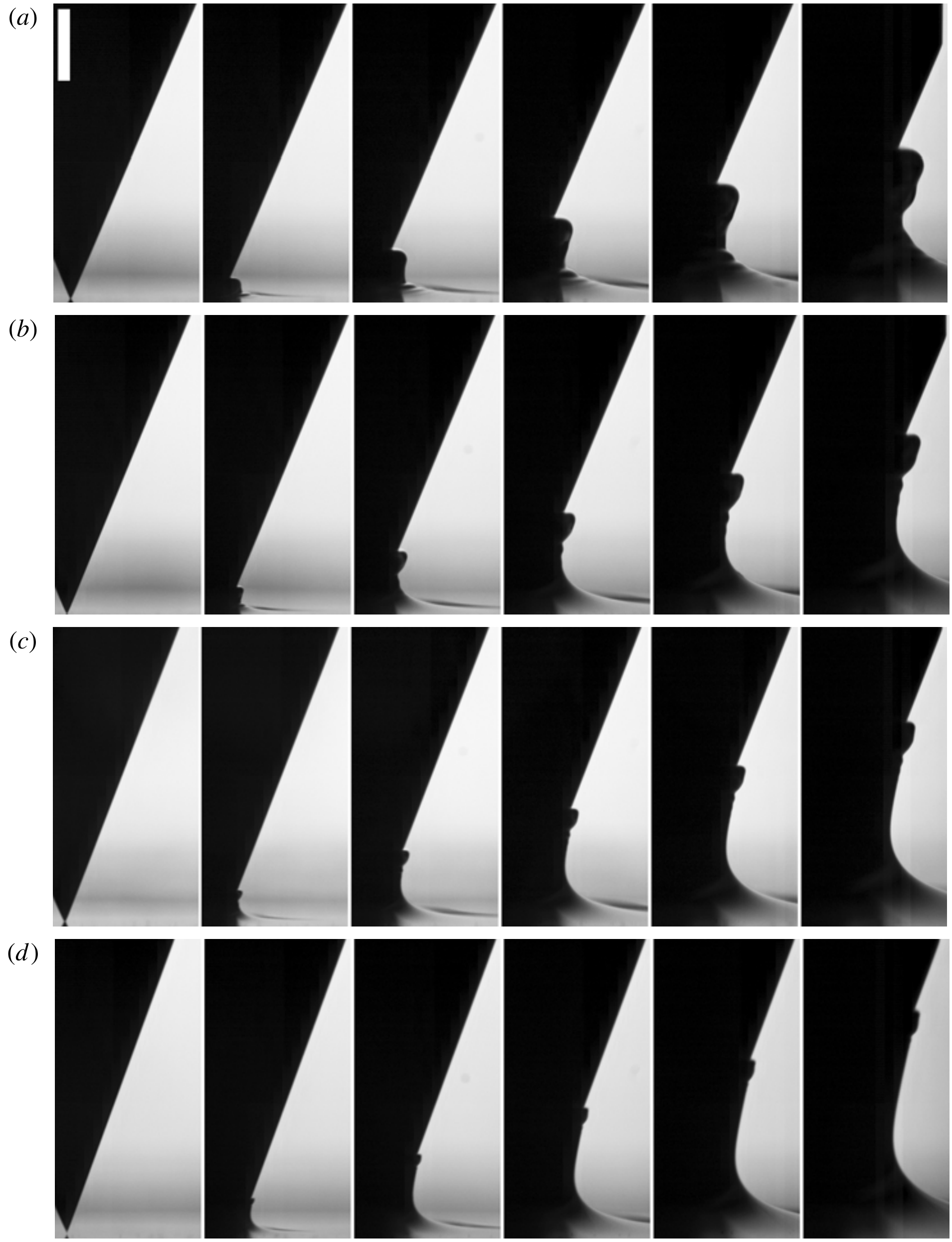

FIGURE 6. The effect of cone impact speed on the ejecta shape. Frames taken from high-speed video clips for the impact of the same 45° cone onto water at different impact speeds: (*a*) $V_c = 1.26\ \mathrm{m\ s^{-1}}$, (*b*) $V_c = 2.16\ \mathrm{m\ s^{-1}}$, (*c*) $V_c = 3.21\ \mathrm{m\ s^{-1}}$ and (*d*) $V_c = 4.95\ \mathrm{m\ s^{-1}}$. The first frame in each sequence shows the frame just before contact and the interval between frames is: (*a*) 6.67 ms, (*b*) 4 ms, (*c*) 2.67 ms and (*d*) 1.67 ms. The vertical distance travelled between frames is therefore about the same ~ 8.4 mm. The view in each frame is shifted to the right to focus on the shape of the free surface. The scale bar represents 5 mm.

and separate the solid and the liquid. In general, these correlations take the form of $V_{ae} \approx \mu^a \sigma^b$, where $a < 0$ and $b > 0$ (see, for example, Burley & Kennedy 1976; Burley & Jolly 1984; Gutoff & Kendrick 1987; Ghannam & Esmail 1993). In particular, we note that the work of Simpkins & Kuck (2003), whereby cylindrical fibres were drawn through liquid baths, resulted in the following correlation:

$$V_{ae} = \left(\frac{\sigma}{\rho}\right)^{0.82} \left(\frac{\mu}{\rho}\right)^{-0.76} \tag{3.1}$$

which yields a threshold air entrainment speed of $V_{ae} = 14.5$ m s^{-1} for water. Even for the highest impact speed shown in figure 6 with $V_c = 4.95$ m s^{-1} shown in figure 6(*d*), the relative contact line speed, which is the total distance the contact line travels along the cone divided by time, $V_{rcl} = 6.2$ m s^{-1}, is below this threshold and, for water, we therefore do not expect any air entrainment through the contact line and thus the appropriate boundary condition for the motion of the liquid along the cone is that of no-slip. Also, the total time from first contact to the final frames of figure 6 are (*a*) 33 ms, (*b*) 20 ms, (*c*) 13 ms and (*d*) 8.3 ms, corresponding to viscous length scales of $L_\nu = \sqrt{\nu t} = 180$, 140, 115 and 90 µm, respectively. This is much smaller than the ejecta thickness on the cone and indicates that viscous effects are negligible over most of its thickness, i.e. outside the boundary layer during the initial ejecta evolution in this case.

Figure 7 shows four realisations for similar cone impact speeds, $V_c \simeq 3.1 \pm 0.1$ m s^{-1}, and liquid viscosities, $\mu = 1$–2.9 mPa s, but a wide range of surface tensions, $\sigma = 72$, 48.1, 30.2 and 11.9 mN m^{-1}, using water, ethanol mixtures and PP1. The corresponding capillary numbers for these realisations are (*a*) $Ca = 0.045$, (*b*) $Ca = 0.15$, (*c*) $Ca = 0.29$ and (*d*) $Ca = 0.28$, again showing that viscous forces should be small during the initial ejecta motions for all cases. The threshold air entrainment velocities based on (3.1) are $V_{ae} = 14.5$ m s^{-1} for water, 5.75 m s^{-1} for 16 % ethanol, 3.2 m s^{-1} for 50 % ethanol and 2.99 m s^{-1} for PP1, whilst the relative contact line speeds are $V_{rcl} = 3.67$ m s^{-1}, 3.9 m s^{-1}, 3.73 m s^{-1} and 3.67 m s^{-1}.

Thus, for figure 7, $V_{rcl} > V_{ae}$ for both 50 % ethanol and PP1. Whilst the images for 50 % ethanol clearly show ejecta detachment, the tip of the ejecta for PP1 does also appear unstable as it travels further up the cone. The detachment is more readily observed from the zoomed images in figure 8. The grey arrows in these frames point to the possible air layer between the cone edge and the ejecta. Further examples of ejecta detachment are shown in figure 9 for the highest impact speeds attained for each respective liquid.

It is tempting therefore to attribute the ejecta detachment to the common air entrainment phenomena; however, this approach clearly neglects the influence of cone wettability and cone angle, both of which are shown herein to influence ejecta detachment.

3.3. *Influence of viscosity*

In figure 10 we compare sequences for the same impact velocity, $V_c \simeq 3.95$ m s^{-1}, while increasing liquid viscosity with (*a*) $\mu = 0.96$ mPa s, (*b*) $\mu = 8.1$ mPa s and (*c*) $\mu = 52$ mPa s. For the water, $V_{rcl} = 2.61 < V_{ae}$ and the ejecta remains attached, whereas for the intermediate viscosity, $V_{rcl} = 2.7 > V_{ae} = 2.0$ m s^{-1} and the ejecta tip is clearly detached.

For the most viscous case, shown in figure 10(*c*), despite the fact that $V_{rcl} = 2.13 > V_{ae} = 0.67$ m s^{-1}, we do not see any separation. We estimate the thickness of the

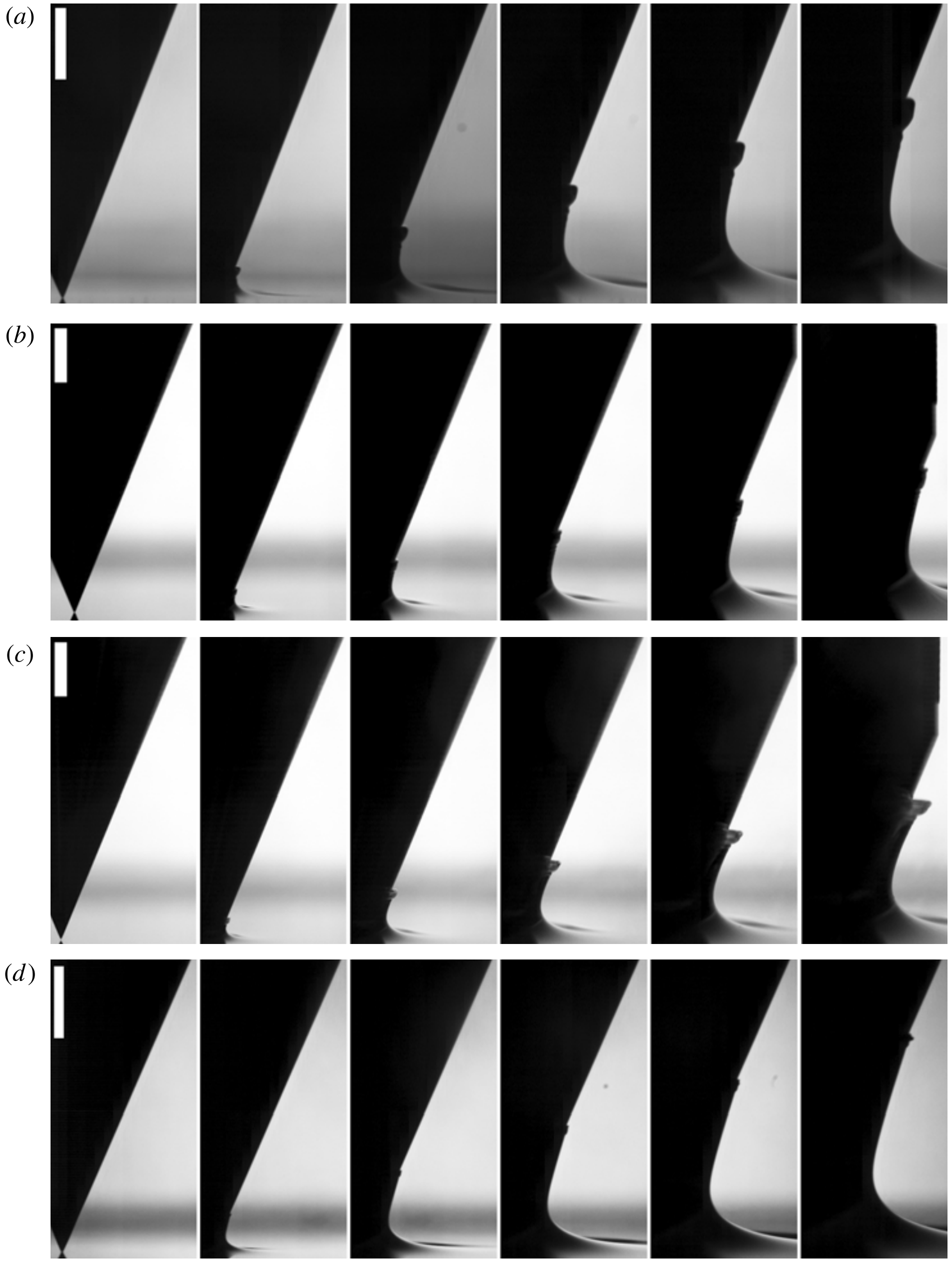

FIGURE 7. The influence of surface tension on the ejecta shapes. Frames from the impact of a 45° cone onto different liquids, at similar impact velocities: (*a*) water, $\sigma = 72$ mN m^{-1}, $V_c = 3.21$ m s^{-1}; (*b*) 16 % ethanol in water, $\sigma = 48.1$ mN m^{-1}, $V_c = 3.27$ m s^{-1}; (*c*) 50 % ethanol in water, $\sigma = 30.2$ mN m^{-1}, $V_c = 3.01$ m s^{-1}; and (*d*) PP1, $\sigma = 11.9$ mN m^{-1}, $V_c = 3.09$ m s^{-1}. The first frame in each sequence shows the frame just before contact and the interval between frames is 2.67 ms. The scales represent 5 mm.

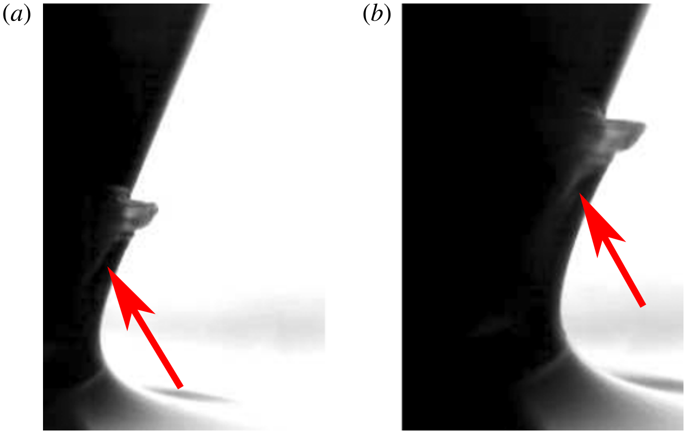

FIGURE 8. Zoomed and contrast-intensified images from the last frames in figure 7(*c*), highlighting the possible entrained air layer between the cone and the ejecta tip. Cone angle is 45°.

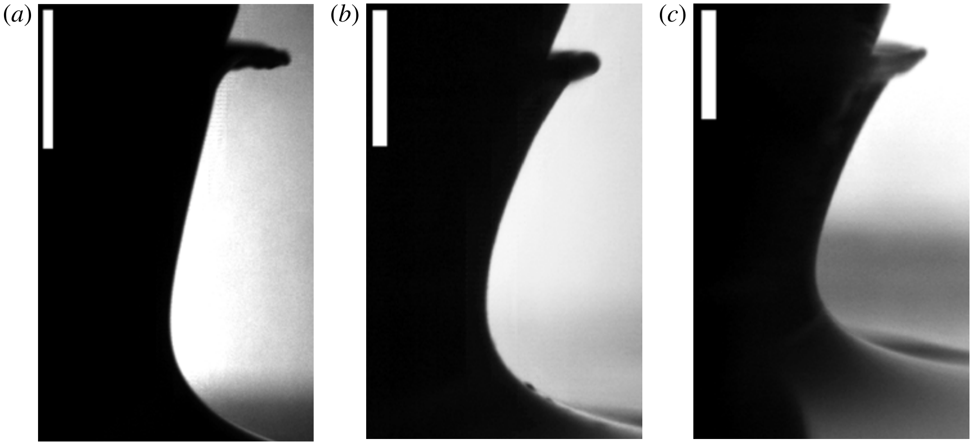

FIGURE 9. Snapshots of the ejecta detachment for (*a*) PP1, (*b*) 50 % glycerol and (*c*) 50 % ethanol. Corresponding capillary numbers are (*a*) $Ca = 0.24$, (*b*) $Ca = 0.47$ and (*c*) $Ca = 0.36$. The scale bars represent 5 mm. Cone angle is 45°.

ejecta tip in the final frames of the video sequence as $\approx 800\ \mu\text{m}$, which coincides with the viscous length scale $L_\nu = \sqrt{\nu t} = 750\ \mu\text{m}$. Even for early times, $t \approx 5$ ms from first contact, the ejecta appears to be no thicker than $\sim 300\ \mu\text{m}$, whilst $L_\nu \approx 470\ \mu\text{m}$. One would therefore expect viscous effects to dominate the motion of the ejecta for this liquid and inspection of the images indeed shows the ejecta to be qualitatively different for this liquid, with no identifiable sheet between the base and the tip of the ejecta.

3.4. *Influence of cone wettability*

Using the superhydrophobic surface treatment detailed in § 2.1, we also performed a series of trials to examine the influence of the cone wettability. Figure 11 compares

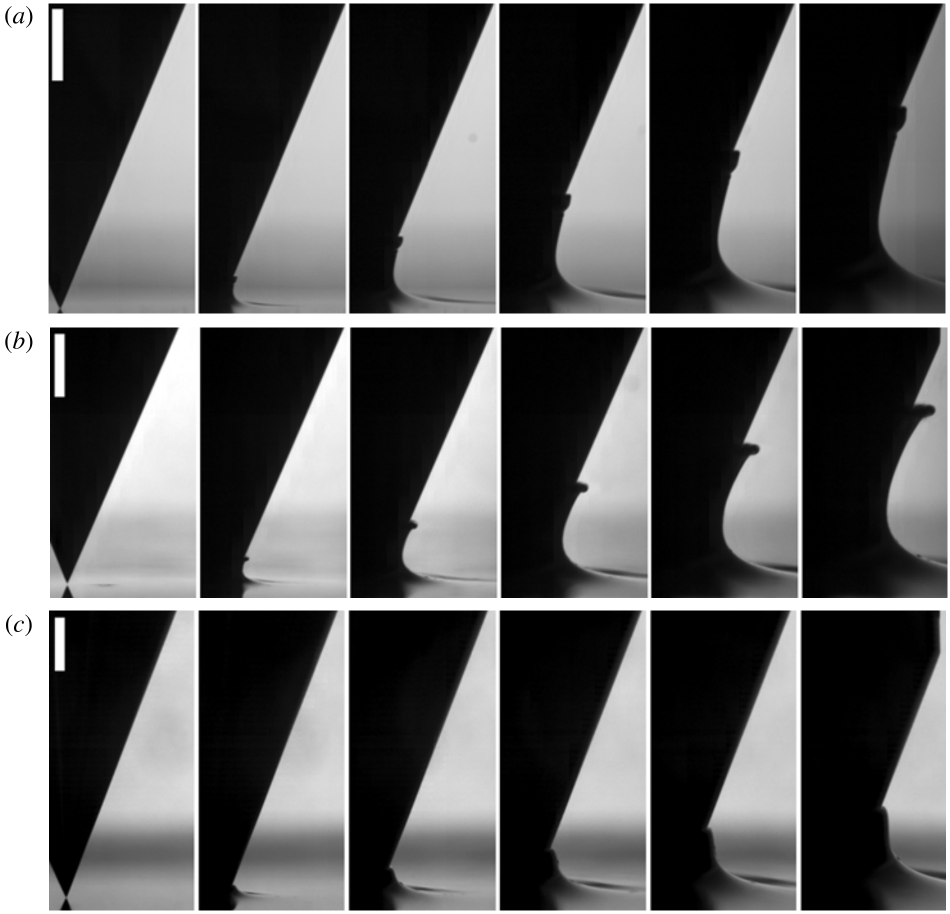

FIGURE 10. The influence of viscosity on the ejecta shape, for similar impact velocity of a 45° cone. High-speed video frames for the impact onto three different liquids: (*a*) water, $\mu = 0.96$ mPa s, $V_c = 3.99$ m s^{-1}; (*b*) 50 % glycerol, $\mu = 8.1$ mPa s, $V_c = 3.94$ m s^{-1} and (*c*) 75 % glycerol, $\mu = 52$ mPa s, $V_c = 3.92$ m s^{-1}. The first frame in each sequence shows the frame just before contact and the interval between frames is 2 ms. The scale bars are 5 mm long.

trials in water for both untreated and superhydrophobic cones for two different impact speeds of $V_c \approx 2$ m s^{-1} (*a*, *b*) and $V_c \approx 4.3$ m s^{-1} (*c*, *d*). In both cases, the hydrophobic cone exhibits more pronounced ejecta tip, indicating the inclusion of an air layer between the surface of the cone and the ejecta itself. The detection of an air layer from high-speed video is typically difficult from side-view silhouettes; however, by using a half-coated cone (coating extends approximately 5 cm up from its tip) and by viewing under the water surface inside the pool, one can easily show that there is indeed a full air layer over the coated section of the solid, as can been seen in figure 12. Here, the upper edge of air layer is seen only in the second and third panels when the liquid reaches the uncoated area, whereupon it breaks down due to physical contact with the cone surface and exhibits a sawtooth-type instability from which air bubbles emanate. This type of instability was also observed on the surface of spheres entering water by Marston *et al.* (2012*b*).

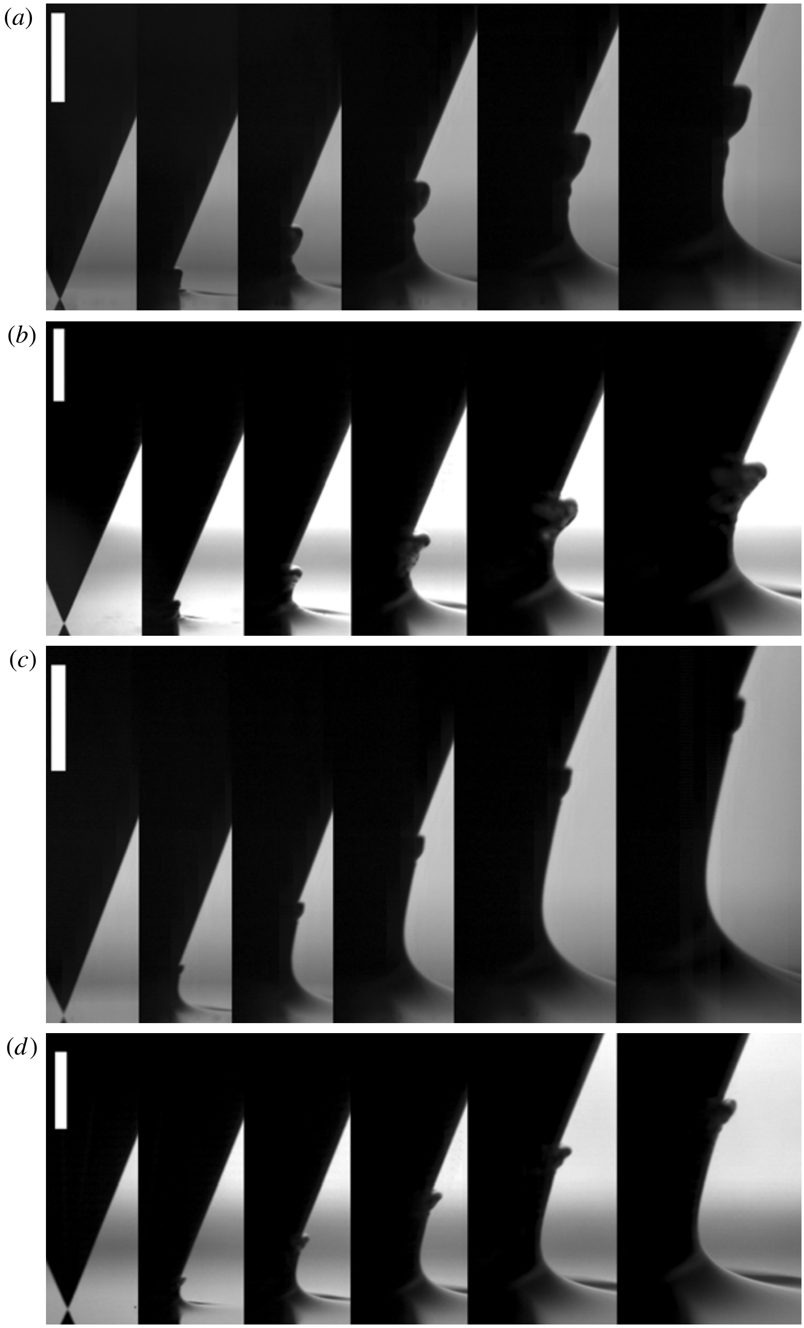

FIGURE 11. Effect of superhydrophobic surface treatment, at two different impact velocities for the impact of a 45° cone onto water: (*a*) untreated cone, $V_c = 2.04$ m s^{-1}; (*b*) superhydrophobic cone, $V_c = 1.96$ m s^{-1}; (*c*) untreated cone, $V_c = 4.38$ m s^{-1}; (*d*) superhydrophobic cone, $V_c = 4.29$. The first frame in each sequence shows the frame just before contact and the intervals between frames are (*a*) 4 ms, (*b*) 4 ms, (*c*) 1.67 ms and (*d*) 1.67 ms. The scale bar in each represents 5 mm.

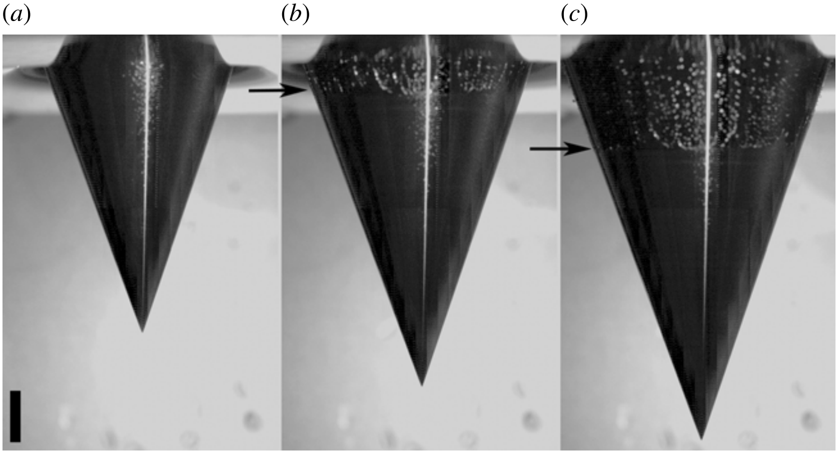

FIGURE 12. Break-up of the entrained air layer viewed from below the liquid free surface. The bottom half of the cone was coated with a superhydrophobic agent in order to stabilise the air layer. The upper edge of the air layer is indicated by the black arrows in (*b*) and (*c*). Frames are separated by 1.3 ms and the scale bar is 1 cm. Here, $V_c = 3.6$ m s^{-1}, $\theta_c = 39°$. See also online supplementary movie 3.

4. Influence of cone angle

4.1. *Straight cones*

To investigate the influence of the cone on the ejecta dynamics, we tested the full range of cones shown in figure 4 each with a range of impact speeds, which we assess in a more quantitative manner in § 5.2. Here, in figure 13, we present snapshots from video sequences for cone angles of $\theta_c = 132$, 79, 39 and 18. The second, third and fourth panels in each sequence represent the various 'wetted' lengths $L_s(t) \approx 8$, 12 and 16 mm calculated from (2.1*a*,*b*). Despite the fact that the ejectas are qualitatively different for each cone angle, the ejecta shapes within any given sequence at these representative times, $\tau = L_s(t)V_c$, do indeed appear to be self-similar (see § 5.1 for a full assessment of this claim). We also clearly see the progressive thickening of the tip of the ejecta with decreasing cone angle and in figure 13(*d*), the ejecta motion is qualitatively different from that seen in figure 13(*a*–*c*).

4.2. *Impact jetting at low deadrise angles*

For small deadrise angles (i.e. large cone angles), we observe fast jets, similar to those first reported by Thoroddsen *et al.* (2004) when spheres first contact a pool of water, in accordance with Wagner theory. Figure 14(*a*) herein shows an example of this phenomena, whereby the jet is ejected from the impact point with a near-horizontal trajectory, but then collides with the pool approximately 1.7 ms from impact (see frame four in figure 15*a*). The early-time jet evolution is shown in figure 14(*b*) (inter-frame times are 100 μs), from which we estimate the initial speed of this jet to be $V_{jet} \approx 21$ m s^{-1}, which gives the ratio $V_{jet}/V_c = 4.6$. Using the length scale in (2.1*a*,*b*), we calculate the Reynolds number at the end of the sequence shown in figure 14(*b*) as $Re = \rho t V_c^2 \tan(\theta_c/2)/\mu = 2.3 \times 10^4$, showing that the jet in this instance is slower than those observed by Thoroddsen *et al.* (2004) at an equivalent Reynolds number for an impacting sphere.

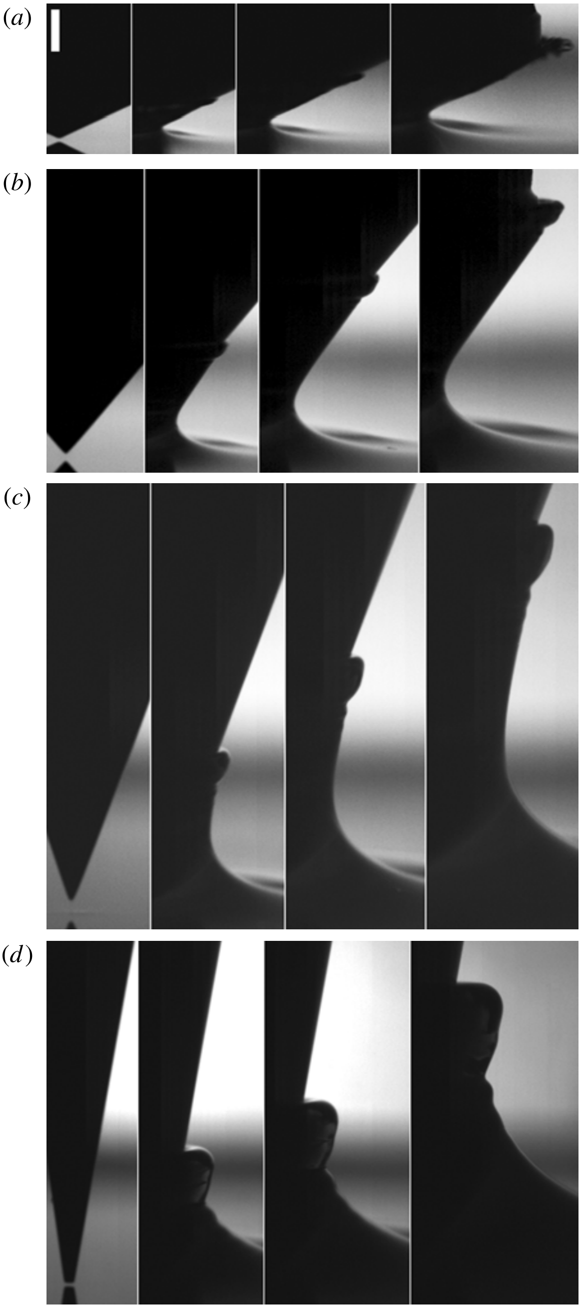

FIGURE 13. Influence of cone angle on the ejecta shape for water. The cone angles and impact speeds shown are: (*a*) $\theta_c = 132.5^\circ$, $V_c = 2.45\ \text{m s}^{-1}$; (*b*) $\theta_c = 79.6^\circ$, $V_c = 2.55\ \text{m s}^{-1}$; (*c*) $\theta_c = 39.3^\circ$, $V_c = 3.17\ \text{m s}^{-1}$; and (*d*) $\theta_c = 18.3^\circ$, $V_c = 2.95\ \text{m s}^{-1}$. The frames shown represent $L_s(t) \approx 0$, 8, 12 and 16, respectively.

Self-similar ejecta shapes would not intersect the pool surface even at later times. We therefore propose that the bending of the ejecta is caused by air drag. A similar

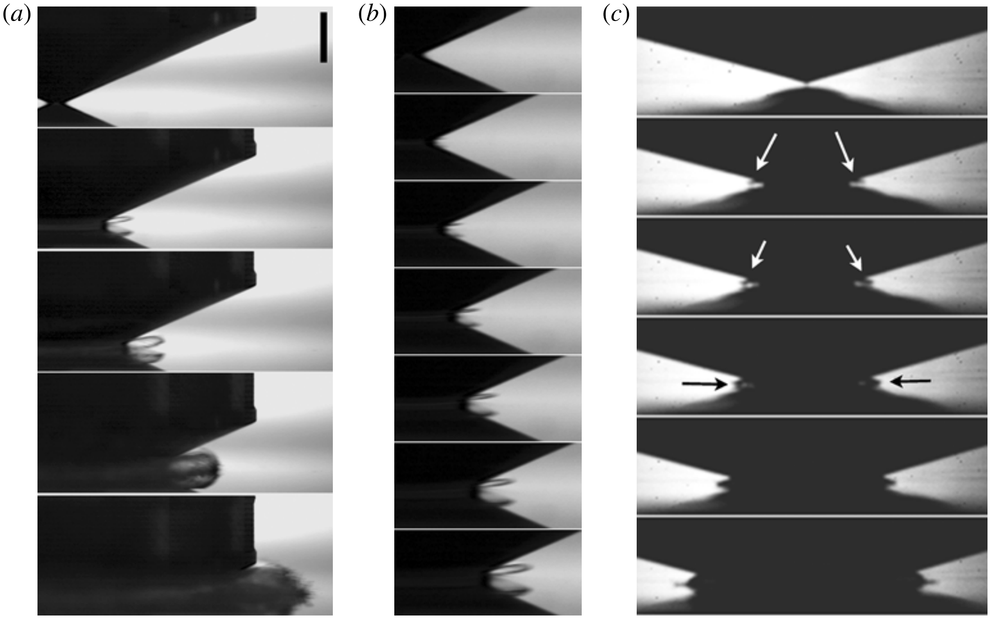

FIGURE 14. (*a*) Ejecta detachment and splashing for a low-deadrise-angle cone, for $\theta_c = 132^{\circ}$, $V_c = 4.55\ \mathrm{m\ s^{-1}}$. The reference scale bar is 1 cm and times of frames from impact are $t = 0.2$, 0.8, 1.1, 1.7 and 2.5 ms. (*b*) Zoomed images at early times showing the high-speed jet formation with the first frame at $t = 0.2$ ms and time intervals of 0.1 ms. See also online supplementary movie 4. (*c*) Early ejecta detachment and contact with the pool surface for $\theta_c = 150^{\circ}$ and $V_c = 7.4\ \mathrm{m\ s^{-1}}$.

behaviour was observed for drop-produced ejecta sheets by Thoroddsen *et al.* (2011), which was eliminated by partially evacuating the ambient air. The ejecta detachment and bending occurs even earlier for higher cone angles and impact speeds, as shown by figure 14(*c*) for $\theta_c = 150^{\circ}$. This makes it challenging to study the evolution of the ejecta for low deadrise angles, as done theoretically by Moore *et al.* (2012), meaning that experiments under reduced air pressure would be called for.

4.3. *Ogive cones*

In addition to the range of straight cones, figure 15 shows two sequences for the curved cones with surface profile radii of curvature (*a*) $r = 25$ mm and (*b*) $r = 62$ mm. In figure 15(*a*), we note that the ejecta has only just reached the edge of the cone when the cone itself comes into contact with the pool, i.e. $L_c(t) \approx 1$, whereby the ejecta is then squeezed between the cone and the pool free surface. Both curved cones show an accelerating ejecta as the effective deadrise angle (excluding the very tip) decreases gradually from approximately 82° to near 0° for $r = 25$ mm and 90° to approximately 40° for $r = 62$ mm, respectively. The frame-by-frame position of the ejecta tip has been plotted in figure 15(*c*), showing that the ejecta for the small curve initially travels away from the pool free surface but reverses direction with respect to the free surface in the final stages as $X \rightarrow 25$ mm. In figure 15(*d*), we plot the temporal evolution of the radial position, X, along with the time-dependent length scale, $L_c(t)$, for both cones. Clearly both cones exhibit an accelerating ejecta

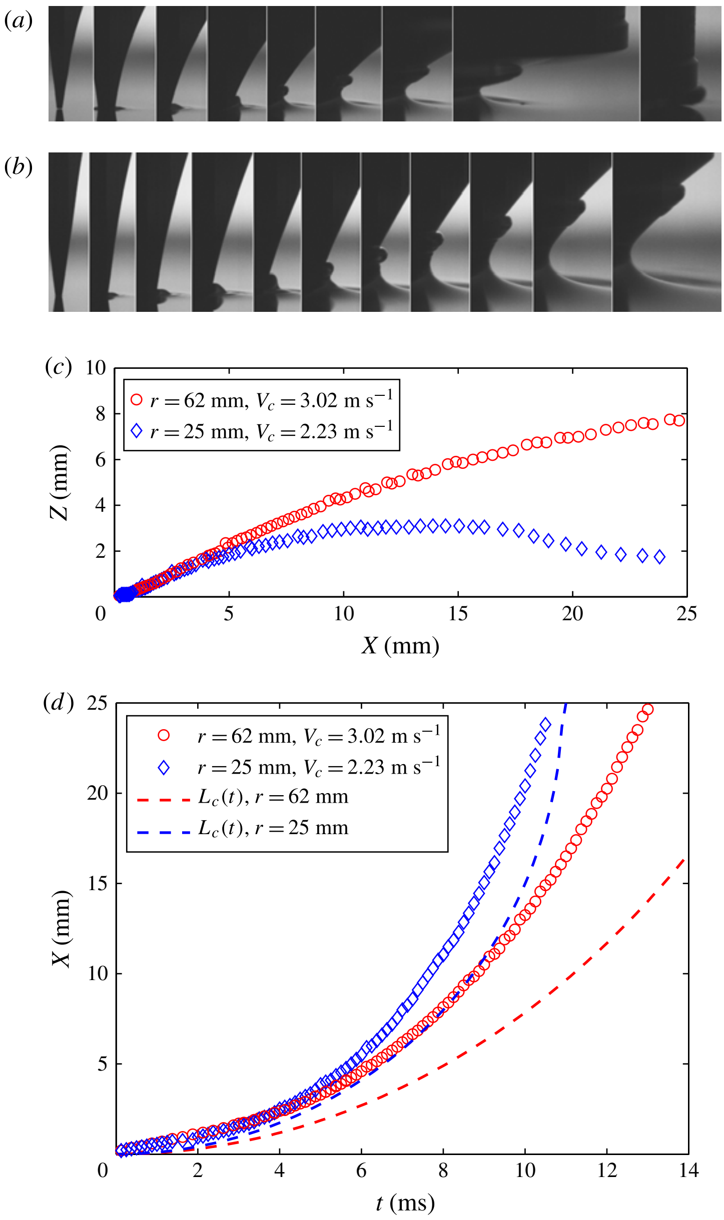

FIGURE 15. Impact of the curved cones onto water (*a*) $r = 25$, $V_c = 2.23$ m s^{-1} and (*b*) $r = 62$, $V_c = 3.02$ m s^{-1}. The first frame is the frame closest to first contact and subsequent frames shown are separated by 1.25 ms. (*c*) Position of the ejecta tip (contact line) extracted through image analysis at one-frame intervals and (*d*) Radial position versus time with corresponding length scale $L_c(t)$ for both cones.

evolution, which is reasonably well described by the simple geometrical length scale $L_c(t)$ for $r = 25$ mm, but not for $r = 62$ mm, where $L_c(t)$ consistently underestimates the true ejecta position by approximately 70 %. Indeed prefactors of 1.3 and 1.7 in (2.1*a*,*b*) render excellent agreement with the experimental data for $r = 25$ and 62 mm,

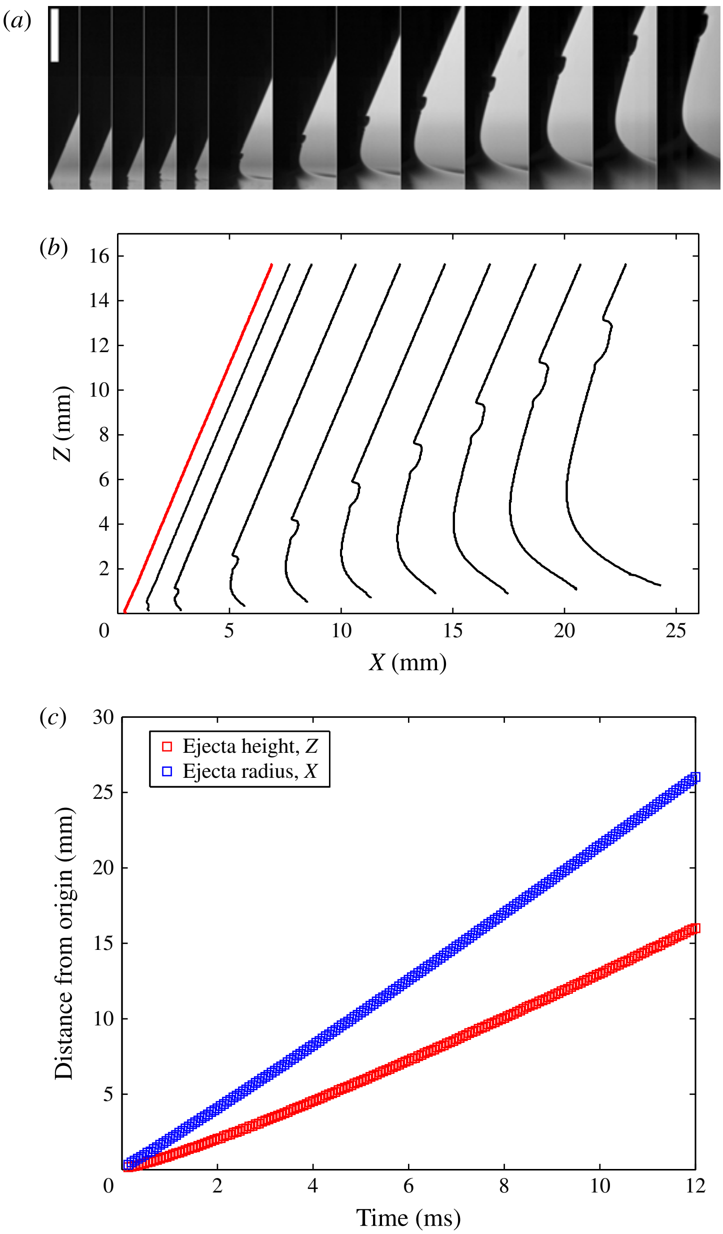

FIGURE 16. (*a*) Time-series from a high-speed video sequence for the impact of a 53° cone at onto water with $V_c = 3.54$ m s^{-1}. The images shown are taken at $t = 0.067$, 0.33, 0.66, 1, 1.33, 2.66, 4, 5.33, 6.66, 8, 9.33, 10.7 and 12 ms after first contact. The scale bar is 5 mm. (*b*) Free-surface shapes determined by image analysis. (*c*) Evolution of the contact line position versus time. In both (*b*) and (*c*), the origin is defined as the point where the cone tip first contacts the water surface.

respectively, and whilst these are purely empirical, we note that the prefactor of 1.3 is very close to $4/\pi$, which is the expected ratio for the true contact line position to the length scale $L_c(t)$ (see De Backer *et al.* 2009).

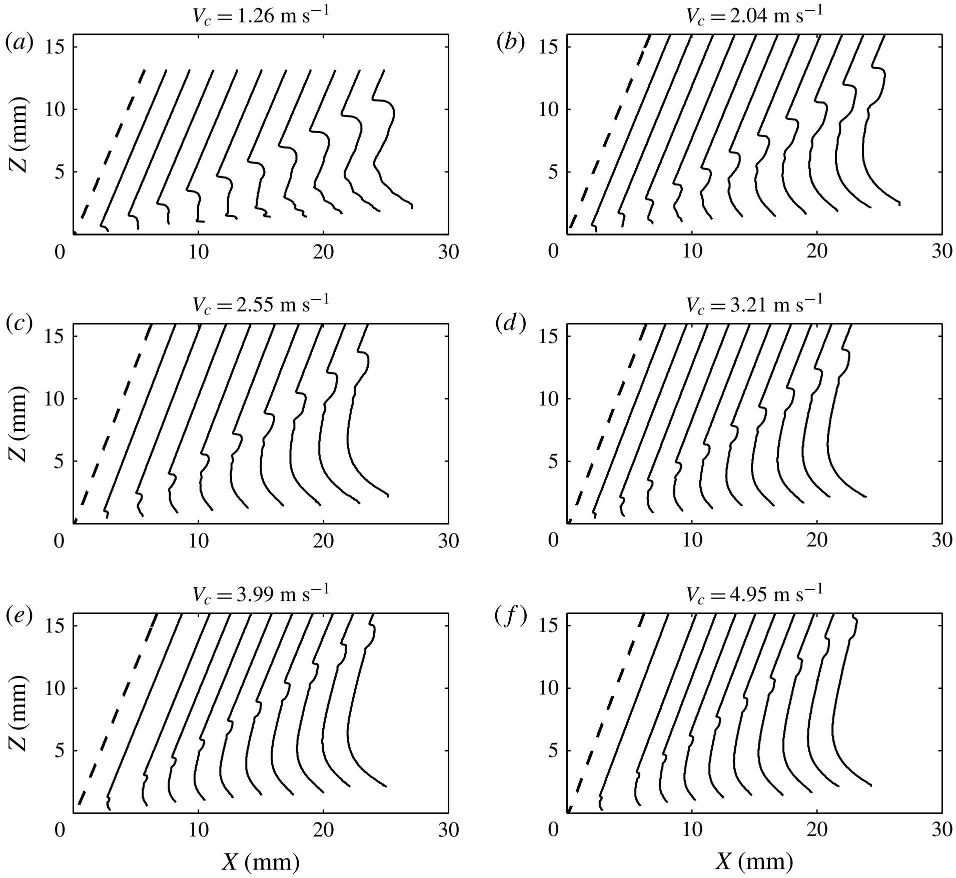

FIGURE 17. Free-surface profiles for impact onto water with $\theta_c = 45°$, for a range of different impact speeds, listed above each panel. The dashed line indicates the cone edge at the moment of impact. Time intervals between shapes are d$t = 3.3$, 2, 2, 1.3, 1 and 0.8 ms, respectively.

5. Early ejecta evolution: scalings and self-similarity

5.1. *Free-surface shapes*

Figure 16 shows select frames (*a*) and subsequent image analysis (*b*, *c*) from a video sequence for impact onto water. First, the ejecta edge from each frame is detected and outlined as in figure 16(*b*), then the radial and vertical position of the contact line are extracted and both plotted as a function of time from impact, as in figure 16(*c*). Free-surface shapes, for the full range of cone impact speeds for a 45° cone impacting onto water are shown in figure 17.

Following from previous studies involving two-dimensional wedge impacts (e.g. Hughes 1972), we then seek to determine whether these profiles for water exhibit self-similarity. Using the simple length scaling tV_c for self-similarity, we can normalise both the vertical and radial coordinates of such profiles. This analysis is shown in figure 18 for the scaled free-surface shapes taken from figure 17 over the full range of impact speeds, $V_c = 1.26$–4.95 m s^{-1}, i.e. showing progressively better collapse as V_c increases. We find that the scaled ejecta shapes at different times, do not collapse

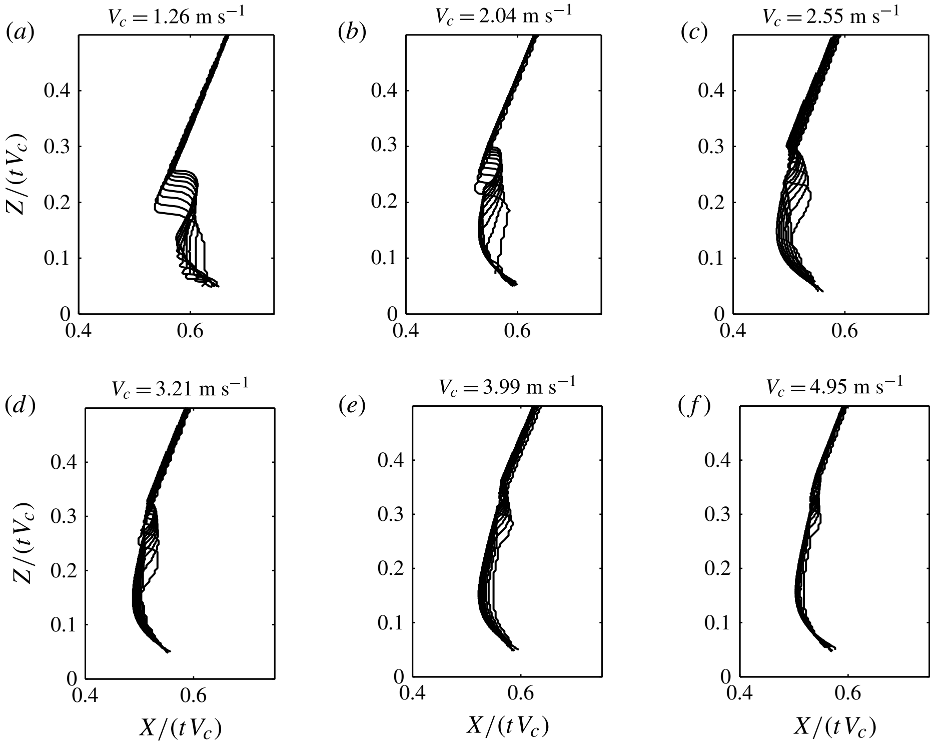

FIGURE 18. Profiles from figure 17 scaled with tV_c. Impact speeds are given above each plot.

well for low impact speeds, but collapse reasonably well for higher impact speeds with $V_c = 3.99$ and 4.95 m s^{-1}, where $Re = \rho t V_c^2 \tan(\theta/2)/\mu = 6.6 \times 10^3 - 8 \times 10^4$ and $Ca = 0.55$–0.069. For these examples, we find the ejecta tip is located at approximately $Z/(tV_c) \approx 0.2$–0.3 and $X/(tV_c) \approx 0.55$.

This analysis is repeated in figures 19 and 20 for PP1, where the ejecta detachment is clearly observed for $V_c = 4.46$ m s^{-1} in figure 19. For this liquid, we find the scaled shapes, shown in figure 20, collapse well even for low impact speeds, whereby $Re = 4.07 \times 10^3$–1.28×10^5 and $Ca = 0.14$–0.41. The fact that the collapse for these profiles is much better than that for water indicates that the liquid physical properties are indeed important. In particular, we note the very low surface tension of PP1, $\sigma = 11.9$ mN m^{-1}, where the kinematic viscosity $\nu = \mu/\rho$ is only 0.65 times that of water.

In light of this, figure 21 presents scaled profiles at various time intervals from different realisations, covering a range of capillary numbers, $Ca = \mu V_c/\sigma = 0.1$–$4$. The fluids used for these realisations were 16 % ethanol, 50 % glycerol and 75 % glycerol solutions. In comparison with figure 20, it is clear that the quality of the collapse is significantly reduced by viscosity, as the collapse in figure 20, for the lowest surface tension fluid herein, is far superior.

5.2. *Radial position of the contact line*

Following from simple geometry (see § 2.2), we propose that the length scale for the intersection of the cone with the undisturbed free surface, $L_s(t) = tV_c \tan(\theta_c/2)$, may

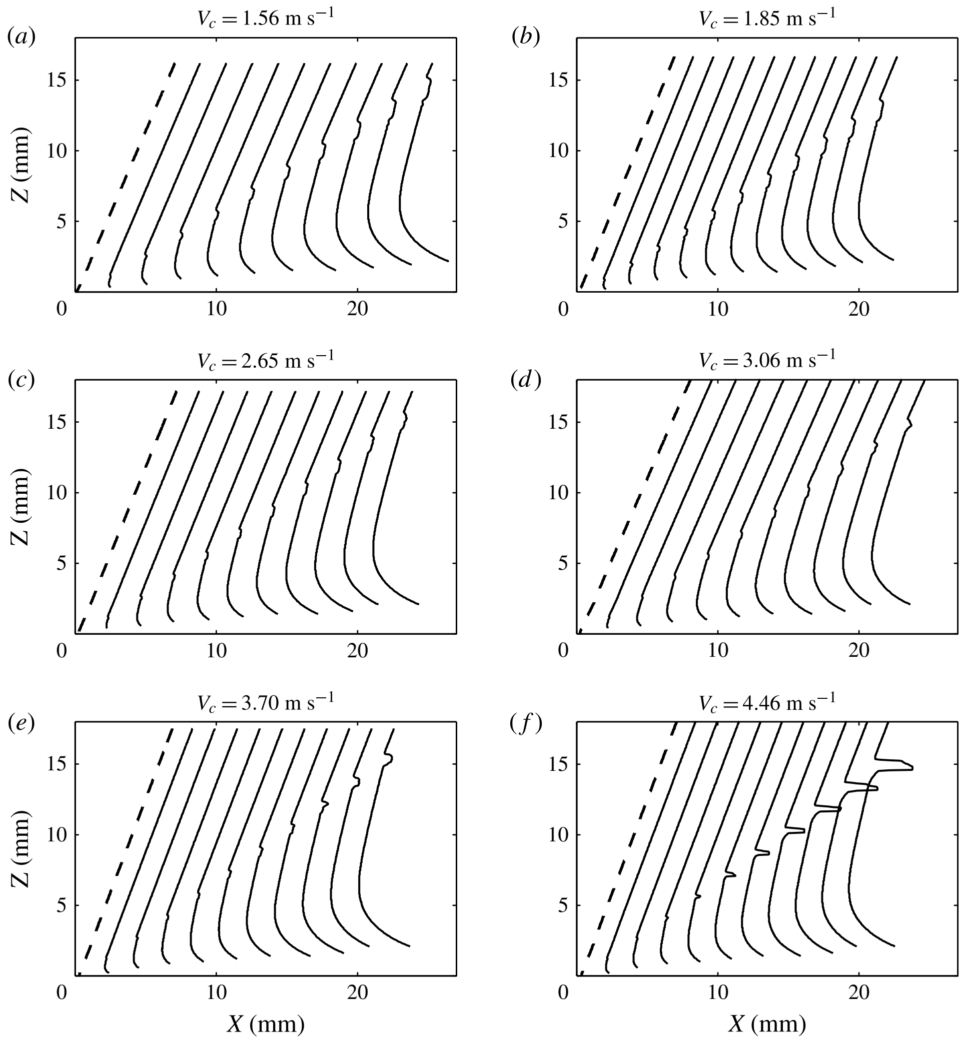

FIGURE 19. Free-surface profiles for impact onto PP1 with $\theta_c = 45°$. Impact speeds are given above each plot. The dashed line indicates the cone edge at the moment of impact. Time intervals between shapes are d$t = 2.66$, 2, 1.66, 1.33, 1.2 and 1 ms, respectively.

be used to scale the radial position of the ejecta tip. Also, following from classical Wagner theory extended to axisymmetric bodies, De Backer *et al.* (2009) state that the ratio of the radial position of the contact line and this length scale should be equal to $4/\pi$. See also Faltinsen (1990) and Howison *et al.* (1991). In figure 22 we plot $X(t)$ versus $L_s(t)$ for multiple trials with impact speeds $V_c = 1.29$–4.95 m s^{-1} onto water, showing that $X(t)/L_s(t) \approx 4/\pi$, in good agreement with the theory. Applying this same scaling to all liquids with this fixed cone angle, shown in figure 23, we find that this ratio holds reasonably well and can be used as a first approximation of the contact line position except for the two water–glycerol solutions shown in figure 23(e,f), where $Ca = 0.12$–0.62 and 0.77–3.92, respectively. This again is an indication of increasing influence of viscous effects, whereby the application of self-similarity no longer holds.

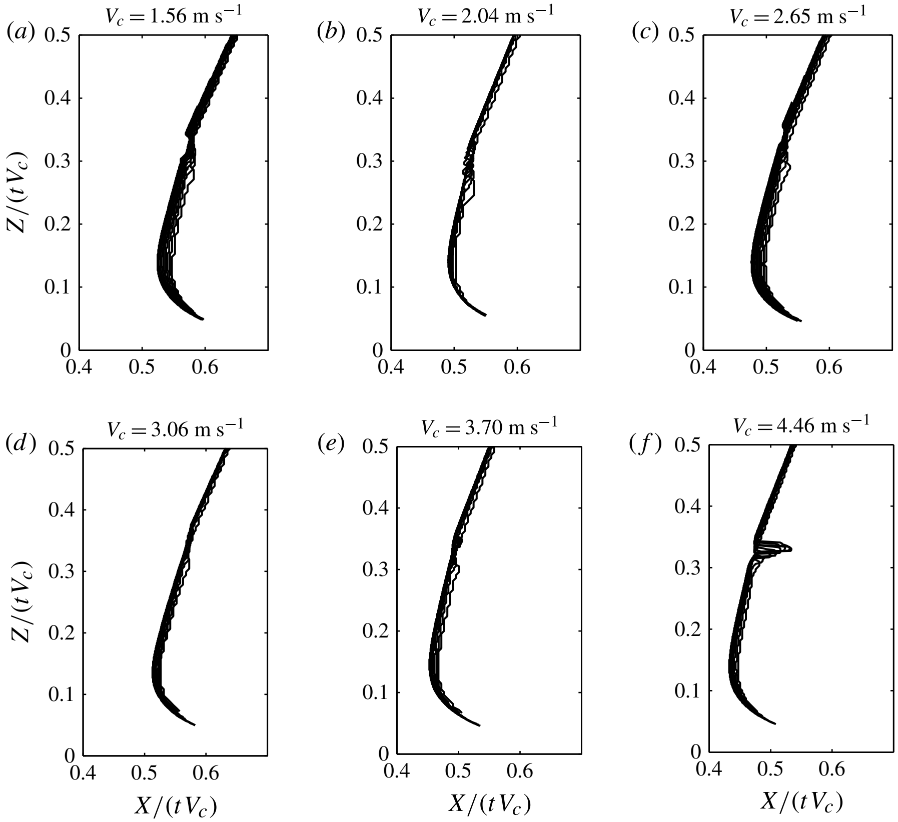

FIGURE 20. Profiles from figure 19 scaled with tV_c. Impact speeds are given above each plot.

In figure 24(*a*), we plot the radial contact line position for all cone angles for similar impact speeds $V_c \approx 3.2$–$3.4\ \mathrm{m\ s^{-1}}$. Attempting to collapse these plots using the radial length scale clearly fails, as shown by figure 24(*b*). Interestingly, the radial length scale collapses the vertical position for the low cone angles, shown in figure 24(*c*), however we note that the high-cone-angle data do not conform. The vertical position of the contact line also cannot be readily scaled by the natural vertical length scale tV_c. We attribute this non-conformance to the fact that the impact speed is too low to be classed as ‘high-speed’, which is main prerequisite cited by Hughes (1972) for self-similarity to occur. This appears to be supported with the data shown in figure 25 where we have examined higher impact speeds using a pure free-fall experimental set-up, rather than the piston. Here all of the data exhibits a better collapse using the simple geometrical scaling, which indicates at least an approach to self-similar evolution of the ejecta at these early times. We postulate that higher impact speeds would indeed render yet better collapse and self-similarity. We note that even for the free-fall set-up, there was negligible deceleration of the cone throughout the early ejecta motions reported herein.

6. Discussions and conclusions

We have performed an experimental investigation of polished stainless steel cone impacts onto quiescent liquid pools. We systematically varied the cone impact speed,

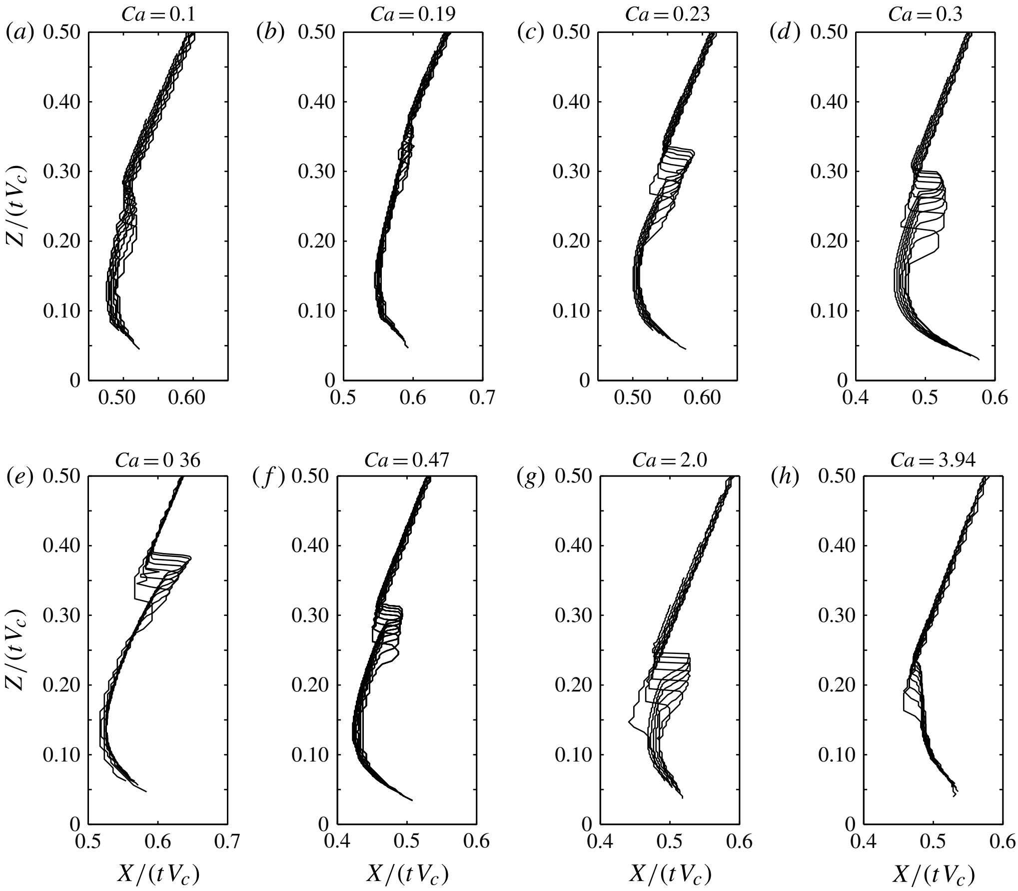

FIGURE 21. Scaled free-surface profiles for various capillary numbers.

cone angle and liquid properties in order to elucidate the dominant physical parameters in the evolution of the ejecta which forms during the earliest stages of the impact. We have observed that for water and other low-viscosity fluids, the ejecta remains attached to the cones as it travels along the length of the cone. However, ejecta detachment was observed to occur for the highest impact speeds for other liquids with higher viscosity or lower surface tension than water. Equally, ejecta detachment during impact onto water was easily promoted by pretreating cones with a hydrophobic coating.

This typically thin ejecta seen for low-viscosity liquids was absent in the highest viscosity liquid tested herein, namely 75 % glycerol ($\mu = 52$ mPa s). In this case, viscous effects dominate as the thickness of the ejecta tip is typically smaller than the viscous length scale $L_\nu = \sqrt{\nu t}$. Thus, it is apparent that ejecta formation is limited by viscosity and, by forming a Reynolds number, $Re = \rho V_c L_s(t)/\mu$, based on the time-dependent length scale, $L_s(t) = tV_c \tan(\theta_c/2)$, we conclude that this ejecta forms only for $Re \geqslant 7000$.

With the aid of image analysis, and by scaling the free-surface shapes with respect to the variable tV_c, we have found that the ejecta for water only exhibits self-similar behaviour for the highest impact speeds, i.e. high capillary and Reynolds numbers. In previous experimental studies, Hughes (1972) showed that the two-dimensional

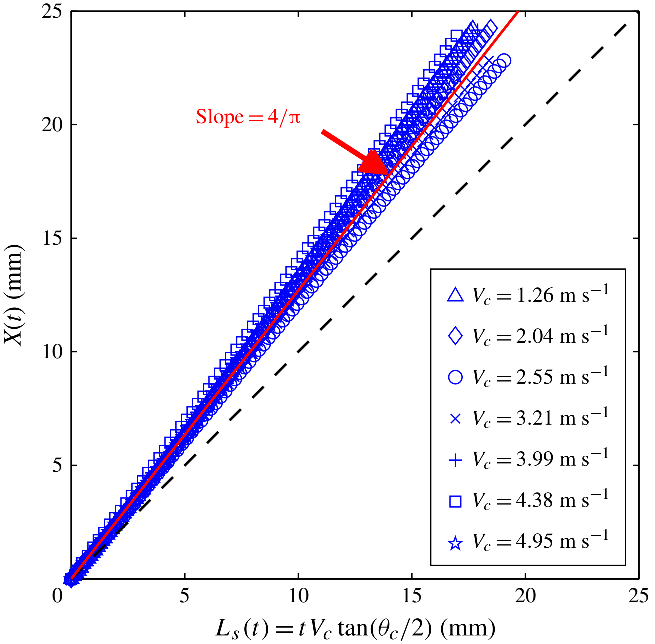

FIGURE 22. Radial position of ejecta tip, $X(t)$, versus geometric length scale $L_s(t)$ for $\theta_c = 45^\circ$ and impact speeds $V_c = 1.26$–4.95 m s^{-1} onto water. The dashed black line indicates parity with the space below this line being unphysical, whilst the red line indicates a slope of $4/\pi$.

self-similar solution of an ideal fluid compared well with experiments only under high-speed impact, when the speed of the wedge is constant during the penetration through the free-surface. This supports our observations that the behaviour is not self-similar at low impact speeds or viscosities much higher than that of water. In contrast, the profiles for the lowest surface tension liquid, namely PP1 exhibit self-similarity at all impact speeds ($N_{pp} = 4.9 \times 10^{-9}$, $Ca = 0.09$–0.46, $Re \approx 7.5 \times 10^3$–$1.5 \times 10^5$). Further comparison of free-surface shapes over a range of capillary numbers ($Ca = 0.1$–4) also indicated that liquid physical properties may also be key ingredients in achieving self-similarity in this phenomenon.

The naturally occurring radial length scale, $L_s(t) = tV_c \tan(\theta_c/2)$, was found to provide a reasonable description of the evolution of the radial position of the contact line for a fixed cone angle of 45° and the ratio of the experimentally determined position, $X(t)$, and $L_s(t)$ was found to be approximately $4/\pi$ which was the ratio originally determined from the extension of Wagner theory to axisymmetric bodies. The exception to this being the two glycerol-based liquids with higher viscosity. Data for the full range of cone angles also failed to collapse. In particular, we note that there is a large discrepancy between cone angles less than 90° and those greater than 90°, where we begin to observe rapid ejecta, and for the highest cone angle (or lowest deadrise angle), we have observed high-speed jets emerging as early as 300 μs from first contact with speeds up to ∼20 m s^{-1}.

Moore *et al.* (2012) indicated that air-cushioning may play an important role in the water entry problem. To comment on this, we refer to our experiments with a superhydrophobic cone (e.g. figures 11 and 12), which induces a full air layer

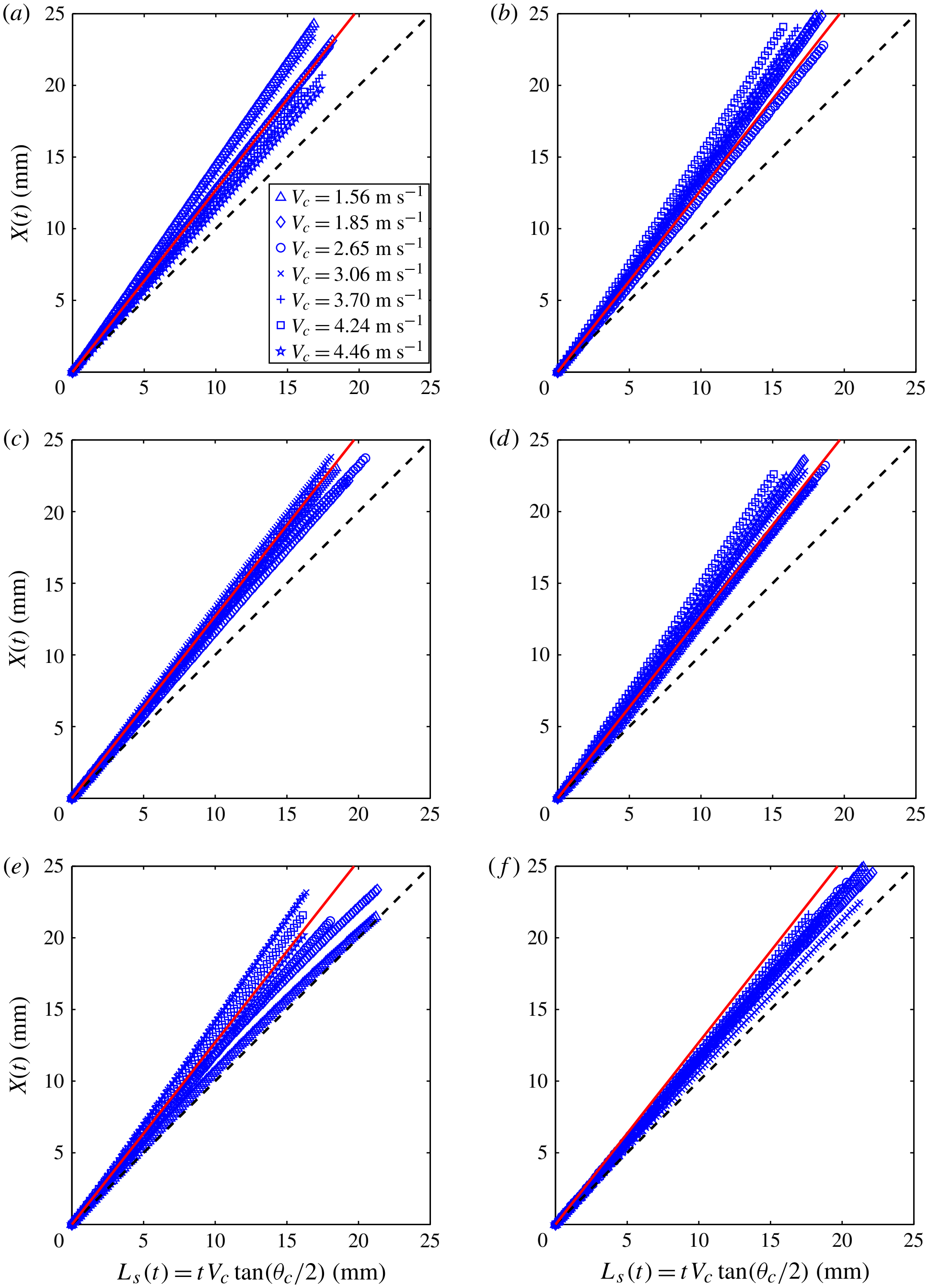

FIGURE 23. Radial position of ejecta tip, $X(t)$, versus the geometric length scale $L_s(t)$ for (*a*) PP1, (*b*) hydrophobic cone onto water, (*c*) 6:1 ethanol, (*d*) 50 % ethanol, (*e*) 50 % glycerol and (*f*) 75 % glycerol. The dashed black line indicates parity with the space below this line being unphysical, whilst the red line indicates a slope of $4/\pi$. Each plot includes data from 21 realisations. The cone angle is $\theta_c = 45^\circ$ and the range of impact speeds is $V_c = 0.99$–5.11 m s^{-1}.

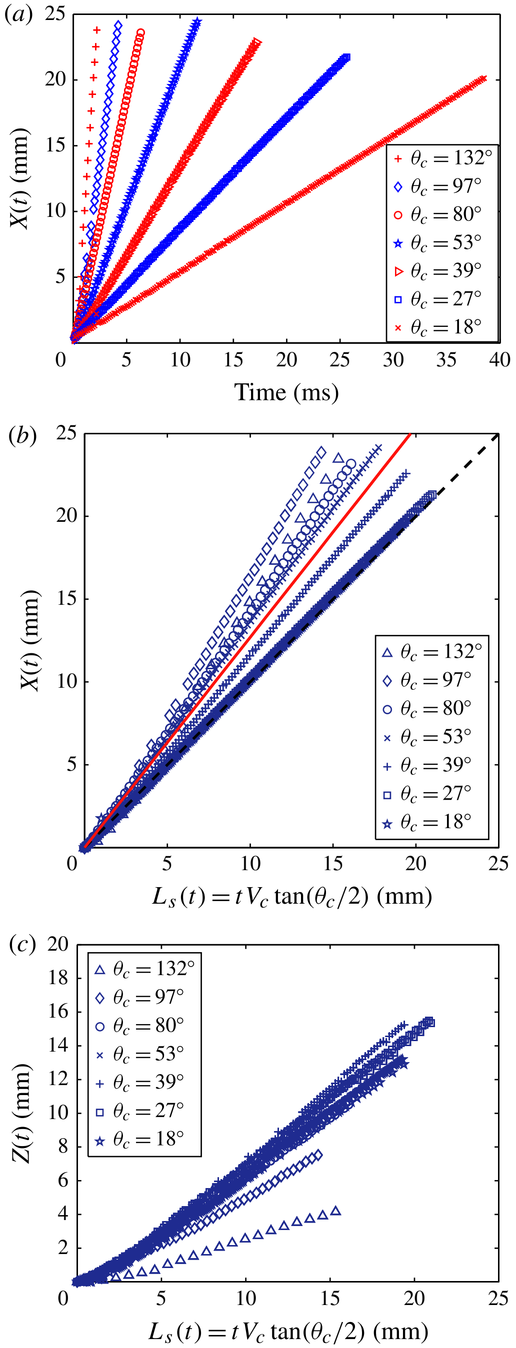

FIGURE 24. (*a*) Radial position of contact line versus time for all straight cones, $\theta_c = 18$–132°, with similar impact speeds all in the range $V_c = 3.2$–3.4 m s^{-1}. (*b*) Data from (*a*) plotted against the radial length scale $L_r(t)$ and (*c*) vertical position of the contact line also plotted against the radial length scale.

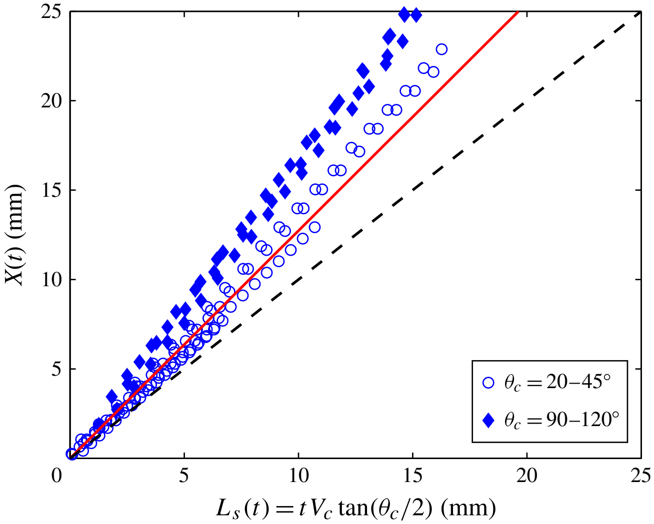

FIGURE 25. Radial position of the contact line for a range of cone angles impacting onto water with impact speed $V_c \approx (2gh)^{1/2} = 7.4$ m s^{-1}, using a free-fall set-up.

between the cone surface and the water and clearly promotes the separation of the ejecta as one might expect. As such, the pressure distribution on the surface of the cone would be fundamentally altered as there is only physical contact between the solid and liquid at peaks of roughness elements, assuming a Cassie–Baxter state. A numerical model which computes the pressure for such a situation may be useful in the future. Experimental extensions of this work could include oblique impacts, to verify the theoretical observations of Moore *et al.* (2012, 2013).

Acknowledgements

We thank K. Takehara and T. G. Etoh at Kinki University for the use of their high-speed cameras during the early stages of this work and J. Oliver and T. Truscott for fruitful discussions. We also thank KAUST for financial support.

Supplementary movies

Supplementary movies are available at http://dx.doi.org/10.1017/jfm.2014.341.

REFERENCES

BALDWIN, J. L. 1971 Vertical water entry of cones *NOLTR* 71-25, available at http://www.dtic.mil/dtic/tr/fulltext/u2/723821.pdf.

BURLEY, R. & JOLLY, R. P. S. 1984 Entrainment of air into liquids by a high speed continuous solid surface. *Chem. Engng Sci.* **39**, 1357–1372.

BURLEY, R. & KENNEDY, S. B. 1976 An experimental study of air entrainment at a solid/liquid/gas interface. *Chem. Engng Sci.* **39**, 1357–1372.

CLANET, C. & VILLERMAUX, E. 2002 Life of a smooth liquid sheet. *J. Fluid Mech.* **462**, 307–340.

DE BACKER, G., VANTORRE, M., BEELS, C., DE PRE, J., VICTOR, S., DE ROUCK, J., BLOMMAERT, C. & VAN PAEPEGEM, W. 2009 Experimental investigation of water impact on axisymmetric bodies. *Appl. Ocean Res.* **31**, 143–156.

DUEZ, C., YBERT, C., CLANET, C. & BOCQUET, L. 2007 Making a splash with water repellency. *Nat. Phys.* **3**, 180–183.

EL MALKI ALAOUI, A., NEME, A., TASSIN, A. & JACQUES, N. 2012 Experimental study of coefficients during vertical water entry of axisymmetric rigid shapes at constant speeds. *Appl. Ocean Res.* **37**, 183–197.

ETOH, T. G., POGGEMANN, D., KREIDER, G., MUTOH, H., THEUWISSEN, A. J. P., RUCKELSHAUSEN, A., KONDO, Y., MARUNO, H., TAKUBO, K., SOYA, H., TAKEHARA, K., OKINAKA, T. & TAKANO, Y. 2003 An image sensor which captures 100 consecutive frames at 1 000 000 f.p.s. *IEEE Trans. Electron. Devices* **50** (1), 144–151.

FALTINSEN, O. M. 1990 *Sea Loads on Ships and Offshore Structures*. Cambridge University Press.

GHANNAM, M. T. & ESMAIL, M. N. 1993 Experimental study of the wetting of fibers. *AIChE J.* **39** (2), 361–365.

GREENHOW, M. 1987 Water entry into initially calm water. *Appl. Ocean Res.* **9**, 214–223.

GUTOFF, E. B. & KENDRICK, C. E. 1987 Low flow limitis of coatability on a slide coater. *AIChE J.* **33**, 141–145.

HOWISON, S. D., OCKENDON, J. R. & WILSON, S. K. 1991 Incompressible water-entry problems at small deadrise angles. *J. Fluid Mech.* **222**, 215–230.

HUGHES, O. F. 1972 Solution of the wedge entry problem by numerical conformal mapping. *J. Fluid Mech.* **56**, 173–192.

IAFRATI, A. & KOROBKIN, A. A. 2004 Initial stage of flat plate impact onto liquid free surface. *Phys. Fluids* **16**, 2214–2227.

JOSSERAND, C. & ZALESKI, S. 2003 Droplet splashing on a thin liquid film. *Phys. Fluids* **15**, 1650–1657.

JUDGE, C., TROESCH, A. & PERLIN, M. 2004 Initial water impact of a wedge at vertical and oblique angles. *J. Engng Maths* **48**, 279–303.

KOROBKIN, A. A. & PUKHNACHOV, V. V. 1988 Initial stage of water impact. *Annu. Rev. Fluid Mech.* **20**, 159–185.

LEWIS, S. G., HUDSON, D. A., TURNOCK, S. R. & TAUNTON, D. J. 2010 Impact of a free-falling wedge with water: synchronised visualization, pressure and acceleration measurements. *Fluid Dyn. Res.* **42**, 035509.

MACKIE, A. G. 1969 The water entry problem. *Q. J. Mech. Appl. Maths* **XXII** (1), 1–17.

MARSTON, J. O., LI, E. Q. & THORODDSEN, S. T. 2012*a* Evolution of fluid-like granular ejecta generated by sphere impact. *J. Fluid Mech.* **704**, 5–36.

MARSTON, J. O., VAKARELSKI, I. U. & THORODDSEN, S. T. 2012*b* Cavity formation by the impact of Leidenfrost spheres. *J. Fluid Mech.* **699**, 465–488.

MOORE, M. R., HOWISON, S. D., OCKENDON, J. R. & OLIVER, J. M. 2012 Three-dimensional oblique water-entry problems at small deadrise angles. *J. Fluid Mech.* **711**, 259–280.

MOORE, M. R., HOWISON, S. D., OCKENDON, J. R. & OLIVER, J. M. 2013 A note on oblique water entry. *J. Engng Maths* **81** (1), 67–74.

SCOLAN, Y.-M. & KOROBKIN, A. A. 2001 Three-dimensional theory of water impact. Part 1. Inverse Wagner problem. *J. Fluid Mech.* **440**, 293–326.

SEMENOV, Y. A. & YOON, B.-S. 2009 Onset of flow separation for the oblique water impact of a wedge. *Phys. Fluids* **21**, 112103.

SHIRTCLIFFE, N. J., MCHALE, G., NEWTON, M. I., PERRY, C. C. & PYATT, B. 2006 Plastron properties of a superhydrophobic surface. *Appl. Phys. Lett.* **89**, 104106.

SIKALO, S., MARENGO, M., TROPEA, C. & GANIC, E. N. 2002 Analysis of impact of droplets on horizontal surfaces. *Exp. Therm. Fluid Sci.* **25**, 503–510.

SIMPKINS, P. G. & KUCK, V. J. 2003 On air entrainment in coatings. *J. Colloid Interface Sci.* **263**, 562–571.

THORAVAL, M.-J., TAKEHARA, K., ETOH, T. G., POPINET, S., RAY, P., JOSSERAND, C., ZALESKI, S. & THORODDSEN, S. T. 2012 von Kármán vortex street within an impacting drop. *Phys. Rev. Lett.* **108**, 264506.

THORODDSEN, S. T. 2002 The ejecta sheet generated by the impact of a drop. *J. Fluid Mech.* **451**, 373–381.

THORODDSEN, S. T., ETOH, T. G., TAKEHARA, K. & TAKANO, Y. 2004 Impact jetting by a solid sphere. *J. Fluid Mech.* **499**, 139–148.

THORODDSEN, S. T., THORAVAL, M.-J., TAKEHARA, K. & ETOH, T. G. 2011 Droplet splashing by a slingshot mechanism. *Phys. Rev. Lett.* **106**, 034501.

VAKARELSKI, I. U., PATANKAR, N. A., MARSTON, J. O., CHAN, D. Y. C. & THORODDSEN, S. T. 2012 Stabilization of Leidenfrost vapour layer by textured superhydrophobic surfaces. *Nature* **489**, 274–277.

WEISS, D. A. & YARIN, A. L. 1999 Single drop impact onto liquid films: neck distortion, jettin, tiny bubble entrapment, and crown formation. *J. Fluid Mech.* **385**, 229–254.

XU, L., ZHANG, W. W. & NAGEL, S. R. 2005 Drop splashing on a dry smooth surface. *Phys. Rev. Lett.* **94**, 184505.

YARIN, A. L. & WEISS, D. A. 1995 Impact of drops on solid surfaces: self-similar capillary waves, and splashing as a new type of kinematic discontinuity. *J. Fluid Mech.* **283**, 141–173.

ZHANG, L. V., TOOLE, J., FEZZAA, K. & DEEGAN, R. D. 2011 Evolution of the ejecta sheet from the impact of a drop with a deep pool. *J. Fluid Mech.* **690**, 5–12.